remote sensing

MDPI

Article

Comparative Study on the Vertical Column Concentration Inversion Algorithm of Tropospheric Trace Gas Based on the MAX-DOAS Measurement Spectrum

Haoyue Wang [1,*], Yuehua Lu [1], Ke Yu [2], Feihong Xiao [1], Rongzhi Guo [1], Naicong Yan [1] and Weiguo Wang [1]

[1] Department of Atmospheric Sciences, Yunnan University, Kunming 650500, China; 110000164664@ynu.edu.cn (Y.L.); xfh1@mail.ynu.edu.cn (F.X.); 12021118004@mail.ynu.edu.cn (R.G.); yannaicong@stu.ynu.edu.cn (N.Y.); wangwg@ynu.edu.cn (W.W.)

[2] Yunnan Meteorological Observatory, Kunming 650032, China; yuke02677628@163.com

* Correspondence: wanghaoyue22@ynu.edu.cn; Tel.: +86-13700667356

Abstract: The tropospheric vertical column concentration (VCDtrop) of NO_2, SO_2, and HCHO was retrieved, respectively, by employing the geometric method (Geomtry), simplified model method (Model), and look-up table method (Table) with the observation spectra of the multi-axis differential absorption spectroscopy instrument (MAX-DOAS). The correlation and relative differences of the inversion results obtained by these three algorithms, as well as the changes in quantiles, were explored. The comparative analysis reveals that the more concentrated the vertical distribution height of gas components is in the near-surface layer, the better the conformity of the VCDtrop retrieved by different algorithms. However, the increase in relative differences is also related to the diurnal variation of gas components. The influence of aerosols on the inversion of the VCDtrop is greater than the change in the vertical distribution height of the gas component itself. The near-surface concentration and distribution height of gas components are the internal factors that give rise to relative differences in the inversion of the VCDtrop by different algorithms, while aerosols are one of the extremely important external reasons. The VCDtrop inverted by Geomtry without considering the influence of aerosols is generally larger except for NO_2. Model sets up aerosols in accordance with the height and meteorological conditions of the atmospheric environment. Table can invert the aerosol profile in real time. Compared with Model, it shows a significant improvement in the refined setting of aerosols. Moreover, while obtaining the vertical distribution of aerosols, it can invert the diurnal variation of the VCDtrop. The VCDtrop inverted by Table is the smallest, and the relative difference with Model is on average about 10% smaller. The relative difference of the VCDtrop for the same height (aerosol optical thickness) quantile is 7–15% (about 25% lower on average). When comparing the inversion results of Table with the Ozone Monitoring Instrument (OMI) satellite product, the MAX-DOAS inversion results of NO_2, SO_2, and HCHO are all larger than the OMI product. This is related to the different observation methods of the MAX-DOAS and OMI and the configuration between the aerosol layer and the distribution height of gas components.

Keywords: multi-axis differential absorption spectroscopy; geometric algorithm; mode simplification method; look-up table method; tropospheric vertical column concentration; the relative differences

check for updates

Citation: Wang, H.; Lu, Y.; Yu, K.; Xiao, F.; Guo, R.; Yan, N.; Wang, W. Comparative Study on the Vertical Column Concentration Inversion Algorithm of Tropospheric Trace Gas Based on the MAX-DOAS Measurement Spectrum. *Remote Sens.* **2024**, *16*, 3359. https://doi.org/10.3390/rs16183359

Academic Editor: Michael Obland

Received: 31 July 2024
Revised: 3 September 2024
Accepted: 3 September 2024
Published: 10 September 2024

Copyright: © 2024 by the authors. Licensee MDPI, Basel, Switzerland. This article is an open access article distributed under the terms and conditions of the Creative Commons Attribution (CC BY) license (https://creativecommons.org/licenses/by/4.0/).

1. Introduction

Using MAX-DOAS technology as a means of optical telemetry, the VCD_{trop} and vertical distribution of trace components (including aerosols) in the troposphere can be effectively obtained by measuring atmospheric scattered radiation at multiple pitching angles [1–5]. Meanwhile, MAX-DOAS can also be equipped with a mobile platform to monitor the spatio-temporal distribution characteristics of trace components at a regional scale. It is helpful in improving the evaluation of air quality and validating the measurement data of different optical telemetry instruments and satellites [6–9]. Compared with other optical

telemetry instruments, MAX-DOAS technology is more suitable for the measurement of trace components with strong chemical activity. Therefore, MAX-DOAS technology has significant developmental advantages and broad application prospects and has positive scientific significance and practical value for the prevention and control of atmospheric environmental pollution.

In recent years, the MAX-DOAS technique has made many important achievements in the inversion of VCD_{trop} and the profile of atmospheric trace components [10–13]. So far, various algorithms such as Geomtry, Model, and Table have been widely used for VCD_{trop} inversion. Good inversion results have been achieved [10,11,14]. Geomtry is the most traditional algorithm for the inversion of VCD_{trop} using the MAX-DOAS technique [2–5,15]. Honninger et al. [16] proposed Geomtry and sought the development prospects of MAX-DOAS technology. Ma et al. [17] applied Geomtry to obtain the VCD_{trop} of NO_2. Wang ting et al. [18,19] retrieved the VCD_{trop} of NO_2 in ultraviolet and visible bands by means of MAX-DOAS observation data combined with Geomtry and analyzed the characteristics of diurnal and seasonal variations of NO_2. Fu Qiang et al. [20] inverted the VCD_{trop} of NO_2 through the independently developed Model. Wu Fengcheng et al. [21] applied vehicle-mounted MAX-DOAS technology to the VCD_{trop} measurement of NO_2 and pointed out that there was a certain difference between satellite monitoring and vehicle-mounted MAX-DOAS inversion results in high-pollution areas, but that there was a good consistency between the two data changes in clean areas. Wagner et al. [5] and Li et al. [22], respectively, locked the trace components required for inversion on multiple distribution parameters and proposed the inversion algorithm of Table. Table uses synchronous measurement of MAX-DOAS to obtain aerosol profiles and inverts VCD_{trop} and vertical distribution on this basis. Li et al. [23] was the first to use Table to invert an aerosol extinction profile. Vlemmix et al. [13] used Table and the Optimal Estimation method (OEM) to invert the VCD_{trop} and the profile of NO_2 and HCHO.

As the MAX-DOAS technique is highly sensitive to the radiative absorption of trace components in the troposphere and boundary layer, the optical radiation characteristics of the VCD_{trop}, profiles, and aerosols can be obtained via inversion algorithms. However, there is heterogeneity and disparity in the inversion processes of different algorithms, which will have an inherent uncertainty impact on the consistency and accuracy of the inversion results. Few existing studies involve quantitative evaluation of the inversion results of different algorithms, and there is even a lack of a relatively comprehensive and systematic description of the differences between algorithms. In particular, the absence of detailed comparative analysis of the relative differences between the inversion results of different algorithms makes it difficult to precisely understand the atmospheric pollution process. Therefore, this paper focuses on comparing the inversion of trace gas VCD_{trop} by three algorithms. In particular, Geometry, Model, and Table are utilized to compare and analyze the relative differences in the inversion results of the VCD_{trop} for NO_2, SO_2, and HCHO based on MAX-DOAS observation spectra and to explore the possible causes for the deviations. It is expected to provide a valuable reference for obtaining accurate tropospheric trace gas compositions and describing the atmospheric pollution process through different inversion algorithms of MAX-DOAS technology.

2. Processing of Spectral Data

Clear sky spectral data of 250~435 nm scattered radiation measured by MAX-DOAS at 9 pitching angles of 2°, 3°, 5°, 7°, 10°, 15°, 20°, 30°, and 90° from July to December 2017 at Fudan University (Qingpu, Shanghai) observation station (31.12°N, 121.06°E, altitude 10 m) were selected. The spectral resolution was 0.5 nm (FWHM). Table 1 lists the configuration of NO_2 and O_4 and HCHO and SO_2 differential oblique column concentration (DSCD) inversions of the measured data based on QDOAS spectroscopy software version 3.2. DSCD contains information on tropospheric oblique column concentration (SCD_{trop}) and stratospheric oblique column concentration (SCD_{strat}).

Table 1. Configuration of NO_2 and O_4 and HCHO and SO_2 differential oblique column concentration inversions by QDOAS spectroscopy software version 3.2.

Target Gas	Interfering Gas	Temperature (K)	Source of Absorption Cross-Section Data [a]	Inverted Wavelength (nm)
NO_2, O_4	O_4	293	Thalman Volkamer (2013)	338~370
	HCHO	298	Meller Moortgat (2000)	
	BrO	224	Fleischmann (2004)	
	NO_2	294, 220	Vandaele (1998)	
	O_3	223, 293	Serdyuchenko (2014)	
	Ring	—	QDOAS	
HCHO	O_4	293	Thalman Volkamer (2013)	338~357
	HCHO	298	Meller Moortgat (2000)	
	BrO	224	Fleischmann (2004)	
	NO_2	294, 220	Vandaele (1998)	
	O_3	223, 293	Serdyuchenko (2014)	
	Ring	—	QDOAS	
SO_2	O_3	223, 293	Serdyuchenko (2014)	305~317.5
	SO_2	293	Bogumil (2003)	
	NO_2	294, 220	Vandaele (1998)	
	HCHO	298	Meller Moortgat (2000)	
	Ring	—	QDOAS	

[a]: http://satellite.mpic.de/spectral_atlas/cross_sections/, accessed on 1 December 2021.

After the fitting with QDOAS, we performed quality control on the fitting results by considering the root mean square (RMS) and the ratio of error to differential slant column density (dSCD).

At noon, the path of scattered light across the atmosphere was the shortest, and a spectrum measured by MAX-DOAS was selected as the reference spectrum. The differential oblique column concentration (DSCD) in the direction of the separation axis, that is, the difference between the DSCD in the direction of different elevation (α) and the DSCD in the direction of 90° elevation of the zenapex, is the differential oblique column concentration ($DSCD_{\alpha,\,trop}$) in the troposphere. NO_2, SO_2, and HCHO are important gas components affected by human activities in the near formation. It has been assumed that the absorption of stratospheric gases in the zenith elevation direction of 90° is equal to that in other α elevation directions by MAX-DOAS technique. Information in the troposphere can be obtained after removing stratospheric information of gas composition [24], i.e.,

$$\begin{aligned} &\mathrm{d}SCD_{\alpha,\mathrm{trop}} = DSCD_{\alpha} - DSCD_{90^\circ} \\ &= (SCD_{\alpha} - SCD_{\mathrm{ref}}) - (SCD_{90^\circ} - SCD_{\mathrm{ref}}) \\ &= SCD_{\alpha} - SCD_{90^\circ} \\ &= (SCD_{\alpha,\mathrm{trop}} + SCD_{\alpha,\mathrm{strat}}) - (SCD_{90^\circ,\mathrm{trop}} + SCD_{90^\circ,\mathrm{strat}}) \\ &= SCD_{\alpha,\mathrm{trop}} - SCD_{90^\circ,\mathrm{trop}} \end{aligned} \quad (1)$$

where α is the observed elevation angle, ref is the reference spectrum, and SCD is the concentration of oblique column (the integral of concentration over optical path). SCD can be converted to vertical column concentration (VCD) by atmospheric mass factor (AMF), i.e.:

$$AMF = \frac{SCD}{VCD} \quad (2)$$

The tropospheric oblique column concentrations in different α elevation and zenith 90° directions can be expressed as the following:

$$SCD_{\alpha^\circ,\mathrm{trop}} = VCD_{\mathrm{trop}} \cdot AMF_{\alpha,\mathrm{trop}} \quad (3)$$

$$SCD_{90^\circ,\mathrm{trop}} = VCD_{\mathrm{trop}} \cdot AMF_{90^\circ,\mathrm{trop}} \quad (4)$$

Since the VCD_{trop} is independent of α, the magnitude of VCD_{trop} obtained in the other α elevation direction and the zenith 90° direction is theoretically equal. Equations (3) and (4) can be subtracted:

$$VCD_{\text{trop}} = \frac{dSCD_{\text{trop}}}{dAMF_{\alpha,\text{trop}}} \quad (5)$$

Here, $dAMF_{\alpha,\text{trop}}$ is the difference between AMF of different α elevation and zenith 90° direction, namely tropospheric differential atmospheric quality factor.

3. Inversion Algorithm

3.1. Geometric Method (Geometric)

If the gas components inverted in Geomtry are concentrated in the near formation, and the AMF mainly depends on the observation elevation of MAX-DOAS, then Equation (1) holds [15,25,26], i.e.:

$$AMF_{\alpha,\text{trop}} \approx \frac{1}{\sin\alpha} \quad (6)$$

Since the AMF of troposphere is equal to 1 when the observed elevation is 90°, Equation (1) is substituted into Equation (5) to obtain Equation (2). VCD_{trop} of NO_2, SO_2, and HCHO can be obtained according to Equation (2).

$$VCD_{\text{trop}} = \frac{dSCD_{\text{trop}}}{(\sin^{-1}\alpha - 1)}, \quad \alpha \neq 90^\circ \quad (7)$$

According to the assumption of box-shaped contour line distribution, we divide VCDtrop by the near-surface concentration to obtain the vertical distribution height and quantitatively study the vertical distribution laws of NO_2, SO_2, and HCHO.

3.2. Simplified Model Method (Model)

Model refers to the use of aerosol parameterized types with relatively fixed settings in Model, which divides aerosols into different combinations according to different heights, visibility, relative humidity, and seasons. The extinction coefficient values of different aerosol types, namely aerosol optical thickness (AOD), were simulated using SCIATRAN model. At the same time, concentration profiles of NO_2, SO_2, and HCHO were read from the model to calculate tropospheric AMF_{trop} of the three gas components, and VCD_{trop} was obtained by using Equation (5).

Table 2 shows the setting combination of relative humidity and aerosol parameters in the model. The aerosol type in the boundary layer is set as urban type, and the relative humidity refers to the observation data of Shanghai Hongqiao Airport in the season and the research results of Chen Zhen et al. [27] and Wang Yi et al. [28]. The local tropospheric visibility of the Qingpu observation station is based on the settings of Wang Shanshan [29], while the boundary layer visibility is based on the settings of Duan Yusen et al. [30], Shi Hong [31], Li Yajuan [32], and Yao Jian et al. [33].

Table 2. SCIATRAN model settings of relative humidity and aerosol parameters in different seasons and altitudes.

LOWTRAN Parameterization		
Altitude	**Spring and Summer**	**Autumn and Winter**
Boundary layer 0~2 km	Urban aerosol	Urban aerosol
	Visibility of 10 km	Visibility of 10 km
	Relative humidity is 80%	Relative humidity is 70%
Troposphere 2~10 km	Visibility of 23 km	Visibility of 23 km
	Relative humidity is 80%	Relative humidity is 70%
Stratosphere 10~30 km	Background aerosol	Background aerosol
	Background load	Background load
Middle layer 30~100 km	Standard mesosphere aerosol	Standard mesosphere aerosol

3.3. Look-Up Table Method (Table)

Table requires the establishment of a data set for aerosol extinction coefficient profiles. The prerequisite for obtaining aerosol profile is to assume that the atmospheric components are evenly mixed in the near-surface and the change of aerosol concentration exhibits e exponential decay with altitude. The aerosol extinction coefficient profile is divided into two layers within 15 km [34–36].

Firstly, real-time aerosol extinction coefficient profile that is inverted by O_4 is substituted into the model to calculate the AMF of inverted gas component. Selecting different step sizes for the parameters in Equations (8)–(10) can obtain a data set of aerosol extinction coefficient profiles.

$$E(z) = \begin{cases} \tau \cdot F/H & z \le H \\ \beta \cdot \exp(-z/\xi) & z > H \end{cases} \tag{8}$$

$$\beta = \frac{(1-F)\cdot\tau}{\xi \cdot (e^{-H/\xi} - e^{-15km/\xi})} \tag{9}$$

$$\tau = \int_{0km}^{15km} E(z)dz \tag{10}$$

where $E(z)$ represents aerosol extinction coefficient and is related to the height z, β is an exponential factor, τ is AOD, F is the percentage of aerosol in boundary layer, H is the mixing height of aerosol layer (height of aerosol layer), and ξ is aerosol scale height within the free troposphere. Due to the fact that most aerosol particles mainly distribute below the height of H, the setting of ξ is not sensitive to the inversion result of aerosol [22] and can be set to 5 km (constant). Table 3 shows the selecting range of aerosol profile parameters.

Table 3. Setting up parameterization of aerosol profile data set.

Parameter	Unit	Assignment
Solar zenith angle (SZA)	Degree (°)	Measured value
Relative azimuth	Degree (°)	Measured value
F	—	0.10~1.00 (interval:0.10)
τ	—	0.10~1.00 (interval:0.10)
		1.15~1.30 (interval:0.15)
		1.50~3.00 (interval:0.25)
		3.50~4.00 (interval:0.50)
H	km	0.20~1.20 (interval:0.05)
		1.30~1.50 (interval:0.10)
z	km	0.10~3.00 (interval:0.25)
		3.50~4.00 (interval:0.50)
		5.00~9.00 (interval:1.00)
		11.00~15.0 (interval:2.00)
ξ	km	5
The total number of aerosol extinction coefficient profiles	Strip	5040

Place the obtained aerosol profile data set into the model to calculate the O_4 dAMF simulation values for 8 elevation angles. Then, calculate the vertical column density (VCD) of O_4, and then use Equation (5) to calculate the measured value of O_4 dAMF ($dAMF_{meas}$), i.e.:

$$\rho = \frac{A_V \cdot N}{V} = \frac{A_V \cdot P}{RT} = \frac{6.022 \times 10^{23} \cdot P}{8.314 \times 10^6 \cdot T} \tag{11}$$

$$\rho_{O_4} = (\rho_{O_2})^2 = (C_{O_2} \cdot \rho)^2 = (0.21 \cdot \rho)^2 \quad (12)$$

$$VCD_{O_4} = \int_0^Z \rho_{O_4}(z)dz \quad (13)$$

In this context, P and T represent air pressure (in Pascals, Pa) and temperature (in Kelvin, K), respectively. The number density of air is denoted by ρ, the number density of O_4 is represented by ρ_{O_4}, and C_{O_2} is the mixing ratio of O_2. In other words, meteorological parameters are crucial in the calculation of dAMF.

All of the measured values of O_4 dAMF ($dAMF_{meas}$) need to be compared with O_4 dAMF simulation values ($dAMF_{model}$) of 5040 aerosol scenarios, i.e.:

$$\chi^2(\tau, F, H) = \sum_{\alpha=2^\circ}^{30^\circ} \left(\frac{\overline{dAMF_{meas}(\alpha)} - dAMF_{model}(\alpha)}{\sigma(dAMF_{meas}(\alpha))}\right)^2 \quad (14)$$

In the equation, χ^2 is value function, and the inversion result of aerosol profile is obtained when the minimum value is taken. Considering the potential instability during spectral analysis, the measured values of dAMF can be averaged hourly. $\overline{dAMF_{meas}(\alpha)}$ is hourly average of dAMF measurements and σ ($dAMF_{meas}(\alpha)$) is standard deviation of dAMF measurements.

Finally, place the aerosol profile that was obtained from inverting into the model and read the concentration profile of NO_2, SO_2, and HCHO. Calculate tropospheric AMF of NO_2, SO_2, and HCHO. Then calculate VCD_{trop} of gas components according to Equation (5).

4. Results and Discussion

4.1. The Diurnal Variation of Column Concentration

Taking July 2017 as an example, Figure 1 used diurnal variations of the HCHO VCD_{trop}, NO_2 VCD_{trop}, and SO_2 VCD_{trop}, which were inverted by Geomtry, Model, and Table, respectively. They indicate that the three algorithms have consistency (with differences) in the diurnal variation of VCD_{trop} for the same (different) gas component inversions. The correlation coefficients of the HCHO (NO_2) VCD_{trop} that were inverted by Geomtry/Model, Table/Geomtry, and Model/Table, respectively, are 0.938, 0.638, and 0.563 (0.746, 0.840, and 0.875), and all passed the 99% significance test. The correlation coefficients corresponding to SO_2 VCD_{trop} were 0.927, 0.939, and 0.940, respectively, which also passed the 99% significance test. The HCHO VCD_{trop} inverted by Geomtry is higher than that of Model, and that of Table is the lowest. The NO_2 VCD_{trop} inverted by Geomtry is lower than the others, while the difference between Model and Table is the smallest. The three algorithms have the smallest relative difference in inverting SO_2 VCD_{trop}.

Due to the correlation between the diurnal variation characteristics of gases with strong chemical activity and factors such as solar radiation and environmental meteorological conditions [37], Table 4 shows the HCHO VCD_{trop}, NO_2 VCD_{trop}, and SO_2 VCD_{trop} that were inverted by three algorithms, the downward solar radiation flux (*DSRF*), and the correlation coefficients between diurnal variations in relative humidity (*RH*) and temperature (*T*). The diurnal variations of HCHO VCD_{trop}, NO_2 VCD_{trop}, and SO_2 VCD_{trop} are not only affected by local emissions but also related to changes in solar radiation and environmental meteorological conditions in Figure 1 and Table 4. The HCHO VCD_{trop} exhibits a unimodal diurnal variation from 12:00 to 15:00 (Beijing time, BJT), and it has consistent variation characteristics with solar radiation and temperature but is negatively correlated with relative humidity. At noon, the strong solar radiation and increasing temperature enhance the photochemical reaction of NO_2 results in a short survival time in the atmosphere. Meanwhile, the VCD_{trop} is low and positively correlated with relative humidity. The life of SO_2 in the boundary layer can reach 1–2 days, and it is extremely susceptible to the non-uniformity of the atmosphere, making the diurnal variation of the VCD_{trop} non-significant. However, it can also exhibit a certain trend of single peak and

single valley diurnal variation and is negatively correlated with solar radiation and relative humidity while positively correlated with temperature.

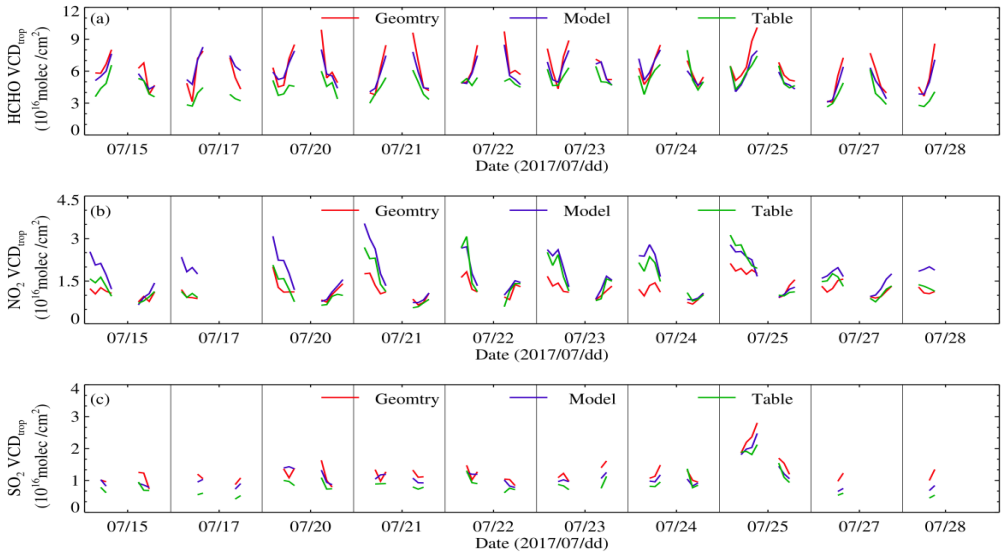

Figure 1. Comparing the diurnal variations of (**a**) HCHO VCD$_{trop}$, (**b**) NO_2 VCD$_{trop}$, and (**c**) SO_2 VCD$_{trop}$ which were inverted by Geomtry (red), Model (blue), and Table (green), respectively, in July 2017.

Table 4. The correlation coefficients for diurnal variation between the HCHO VCDtrop, NO_2 VCDtrop, and SO_2 VCDtrop inverted by Geomtry, Model, and Table and *DSRF*, *RH*, and *T* at the Qingpu observation station in July 2017, which all passed the 99% significance test.

	Geomtry			**Model**			**Table**		
Factor	**HCHO VCD$_{trop}$**	**NO_2 VCD$_{trop}$**	**SO_2 VCD$_{trop}$**	**HCHO VCD$_{trop}$**	**NO_2 VCD$_{trop}$**	**SO_2 VCD$_{trop}$**	**HCHO VCD$_{trop}$**	**NO_2 VCD$_{trop}$**	**SO_2 VCD$_{trop}$**
DSRF	0.564	−0.198	−0.235	0.442	−0.208	−0.065	0.498	−0.152	−0.222
RH	−0.428	0.405	−0.265	−0.361	0.712	−0.205	−0.431	0.531	−0.268
T	0.402	−0.326	0.300	0.322	−0.690	0.284	0.473	−0.452	0.335

Figure 2 shows the diurnal variation characteristics of wind direction and speed at the Qingpu observation station in July 2017. According to the analysis in Figure 1, the wind speed starts to increase at noon, enhancing the atmospheric non-uniformity. The mixing conditions of turbulence and diffusion are good, resulting in an increase in the VCDtrop of HCHO and SO_2 at noon and a decrease in the VCDtrop of NO_2. However, the chemical activity of HCHO, NO_2, and SO_2 varies, and the significant correlation between the VCD$_{trop}$ diurnal variation inverted by the three algorithms and solar radiation as well as meteorological elements is consistent.

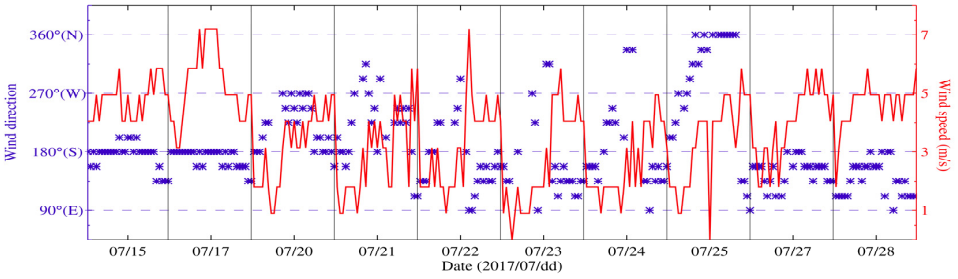

Figure 2. The diurnal variation characteristics of wind direction and speed at the Qingpu observation station in July 2017.

In order to verify the inverted VCD_{trop}, semi-quantitative analysis [38] of gas component concentrations observed synchronously from near the surface can be used. Only the NO_2 VCD_{trop} and SO_2 VCD_{trop} diurnal variations inverted by the three algorithms compared with NO_2 and SO_2 observed synchronously from near the surface are shown in Figures 3 and 4 due to the lack of measurement for the HCHO concentration near the surface. They indicate that the correlation coefficients between the NO_2 VCD_{trop} inverted by Geomtry, Model, and Table and the variation of NO_2 concentration in the near ground are 0.585, 0.823, and 0.888; all passed the 99% significance test. The result displays that the dominant role of near-ground NO_2 concentration in the proportion of NO_2 VCD_{trop} changes and that the NO_2 VCD_{trop} is related to the lower distribution height of NO_2.

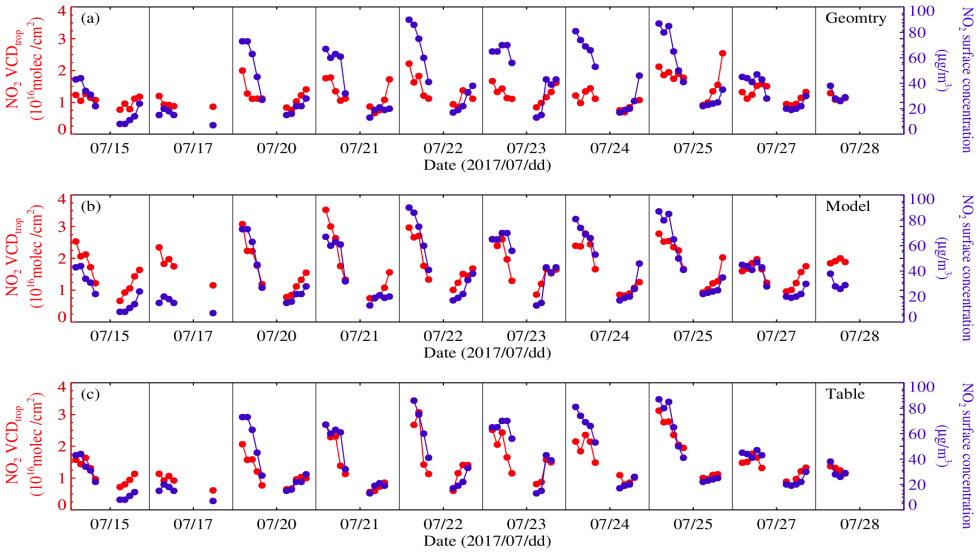

Figure 3. The comparison between the NO_2 VCD_{trop} inverted (red) by (**a**) Geomtry, (**b**) Model, and (**c**) Table, respectively, and the NO_2 observed (blue) synchronously near the surface.

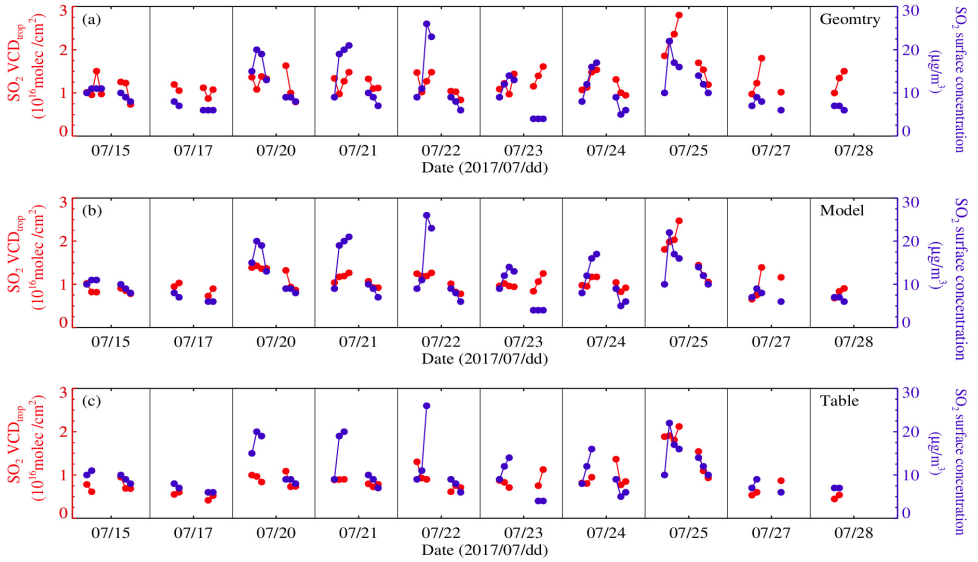

Figure 4. The comparison between the SO_2 VCD_{trop} inverted (red) by (**a**) Geomtry, (**b**) Model, and (**c**) Table, respectively, and the SO_2 observed (blue) synchronously near the surface.

The correlation coefficients between the SO_2 VCD_{trop} inverted by the three algorithms and the variation of SO_2 concentration in the near ground are 0.205, 0.382, and 0.275, also passing the 99% significance test. However, the consistency between the SO_2 VCD_{trop} and

concentration changes of the near-ground SO_2 is not as good as the NO_2. Although the diurnal variation of the SO_2 VCD_{trop} is not significant and only slightly increases at noon, there is still similarity with the diurnal variation of the near-surface SO_2 concentration. It is related to the height of the elevated chimney in the factory as a source of SO_2 emissions. According to the assumption of the box-shaped profile distribution, related information of vertical concentration distribution at different altitudes can be inferred by the matching status between the VCD_{trop} and the near-ground concentration [38], thereby quantitatively obtaining the characteristics of vertical distribution changes of NO_2 and SO_2.

4.2. Seasonal Variation of Column Concentration

Seasonal variations of the HCHO VCD_{trop}, NO_2 VCD_{trop}, and SO_2 VCD_{trop} inverted by Geomtry and the diurnal variation characteristics of the VCD_{trop} for the seasonal averages are shown in Figures 5 and 6. They indicate the seasonal variations of the negative phase between the HCHO VCD_{trop} and NO_2 VCD_{trop} as well as SO_2 VCD_{trop}, and that the diurnal variations of the HCHO VCD_{trop}, NO_2 VCD_{trop}, and SO_2 VCD_{trop} vary between different seasons. The HCHO VCD_{trop} is relatively high (low) in summer (autumn and winter), and the diurnal variation is the largest (stable). The source of HCHO is complex in summer, which includes natural and anthropogenic emissions and photochemical reactions [39,40]. The observation of the near-ground HCHO concentration in Shanghai obtained by an active DOAS system shows the diurnal variation in summer (other seasons) is the largest (smaller) and the concentration relatively enhances (declines) at noon (morning and afternoon) [41], and the HCHO VCD_{trop} measured by MAX-DOAS in summer is also higher than in winter [37].

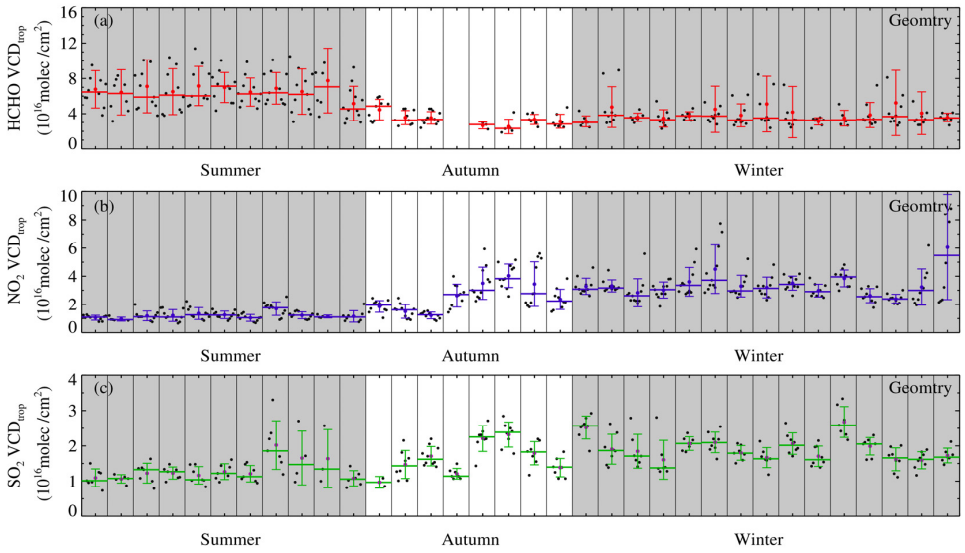

Figure 5. The diurnal variation characteristics of the (**a**) HCHO VCD_{trop}, (**b**) NO_2 VCD_{trop}, and (**c**) SO_2 VCD_{trop} for different season inverted by Geomtry. The black dot represents the hourly average value of the VCD_{trop}; the red, blue, and green dashes represent the median values of the VCD_{trop} for HCHO, NO_2, and SO_2, respectively; and the point on the error bar represents the average value.

The NO_2 VCD_{trop} is higher (lower) in the autumn and winter (summer), and the same seasonal variation characteristics are also exhibited at different observation stations in Shanghai [37,42–44]. The weaker solar radiation in autumn and winter compared to summer cause the photochemical reaction of NO_2 to dwindle, and the lower boundary layer height is conducive to the accumulation of NO_2. The increasing OH radical content strengthens the oxidation of atmosphere, making NO_2 prone to photolysis, and the diurnal variation of the NO_2 VCD_{trop} exhibits a concave distribution. The NO_2 VCD_{trop} is usually prone to highs every morning (afternoon) before work (after work), which is precisely the increase in car exhaust emissions generated during peak commuting hours for people, and

the weaker solar radiation leads to a weakened photolysis reaction and a lower boundary layer height which is conducive to the accumulation of NO_2. The increasing temperature leads to an enhanced boundary layer height that is beneficial for atmospheric diffusion. Meanwhile, the enhancement of solar radiation leads to the photochemical removal of NO_2, resulting in a relatively flat low value of NO_2 VCD_{trop}.

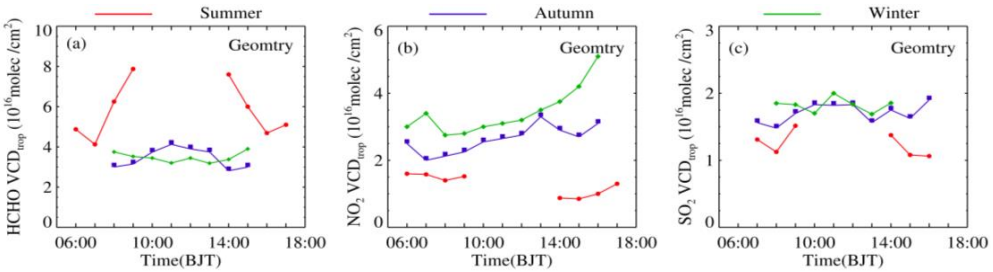

Figure 6. The average diurnal variation for the (**a**) HCHO VCD_{trop}, (**b**) NO_2 VCD_{trop}, and (**c**) SO_2 VCD_{trop} inverted by Geomtry in different seasons. Red, blue, and green represent summer, autumn, and winter, respectively.

The average diurnal variation for the SO_2 VCD_{trop} is lower than that of the NO_2 VCD_{trop} in different seasons. Similar change characteristics can be found from the analysis of observation for MAX-DOAS and the comparison between the concentration of SO_2 and NO_2 near the surface [37]. The SO_2 VCD_{trop} in autumn and winter is higher than that in summer, and it is relatively high only at noon. The SO_2 VCD_{trop} is prone to low values every morning and afternoon which is likely due to the dynamic balance between the photolysis rate, atmospheric heterogeneity, and industrial emissions.

By comparing and analyzing Figures 5 and 6, similar change characteristics also exist between the SO_2 VCD_{trop} and HCHO VCD_{trop} as well as the NO_2 VCD_{trop}, which were inverted by Model and Table, respectively (image omitted).

4.3. Statistic and Analysis

4.3.1. Variation in Relative Differences

We used the most traditional and widely used Geomtry inverted results as a reference to analyze the relative differences of the VCD_{trop} between different algorithms. Figures 7 and 8 show the comparison of statistical characteristics between the HCHO VCD_{trop}, NO_2 VCD_{trop}, and SO_2 VCD_{trop} which were inverted by Model and Table, respectively, and those inverted by Geomtry from July to December 2017. Figure 7 indicates that the frequency with a NO_2 VCD_{trop} less than (greater than) 2.5×10^{16} molec/cm^2 inverted by Model is slightly less (greater) than that by Geomtry. However, the frequency with a SO_2 VCD_{trop} greater than (less than) 1.5×10^{16} molec/cm^2 inverted by Model is less (greater) than that by Geomtry, and the frequency with a HCHO VCD_{trop} less than (greater than) 2.5×10^{16} molec/cm^2 inverted by Model is slightly greater (less) than that by Geomtry. For different frequency distribution changes, the NO_2 (SO_2) VCD_{trop} inverted by Model or Geomtry aggregates within the range of 1.5 to 4.0 (1.0 to 2.0) $\times 10^{16}$ molec/cm^2, while HCHO VCD_{trop} aggregates within the range of 2.0 to 7.0 $\times 10^{16}$ molec/cm^2.

The correlation coefficients of the NO_2 (SO_2, HCHO) VCD_{trop} inverted by Model/Geomtry is 0.865 (0.837, 0.880) which passed the 99% significance test; the slope of the fitting line is 0.914 (0.663, 0.741) and the corresponding intercept is 0.443 (0.230, −0.109). The median relative difference for the VCD_{trop} is 9.69% (−20.34%, −35.35%). When the theoretical values of the NO_2 VCD_{trop} inverted by Geomtry is less (greater) than 5.151×10^{16} molec/cm^2, the inversion values of the corresponding Model are slightly larger (smaller). The relative difference between Model and Geomtry decreases (increases) with the increase of the VCD_{trop}, but the VCD_{trop} inverted by Model is somewhat large. When the SO_2 VCD_{trop} inverted by Geomtry is less (greater) than 0.683×10^{16} molec/cm^2, the inversion values of the corresponding model are slightly larger (smaller). The relative difference between

Model and Geomtry diminishes (increases) with the increase of the VCD_{trop}, but the overall VCD_{trop} inverted by Geomtry is too large. When the HCHO VCD_{trop} inverted by Geomtry is greater than 0.147×10^{16} molec/cm^2, the VCD_{trop} inverted by Model is increasing but is always smaller than that by Geomtry, and the relative difference between Model and Geomtry declines with the increase of VCD_{trop}.

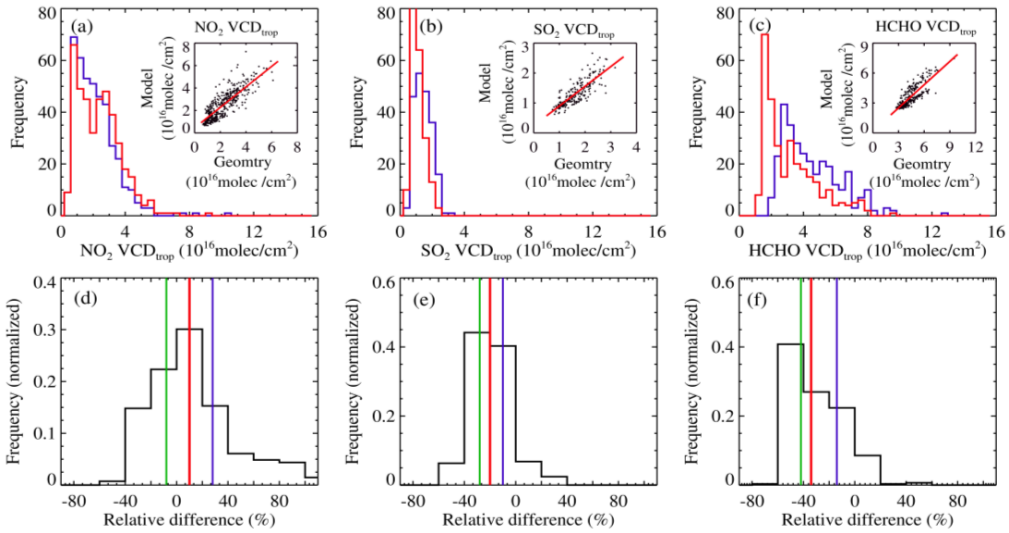

Figure 7. The comparison of statistical characteristics between the HCHO VCD_{trop}, NO_2 VCD_{trop}, and SO_2 VCD_{trop} which were inverted by Model/Geomtry; (**a**–**c**) is the corresponding frequency variations of the VCD_{trop} inverted by Model (red line)/Geomtry (blue line); (**d**–**f**) is the normalized frequency distribution and the 25% (green), 50% (red), and 75% (blue) quantile line of relative differences for the VCD_{trop}.

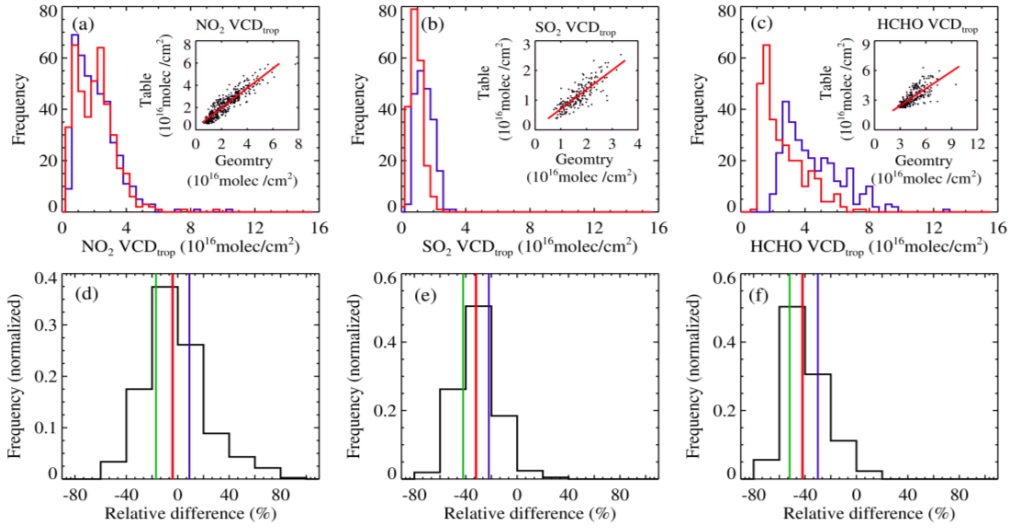

Figure 8. The comparison of statistical characteristics for the NO_2 VCD_{trop}, SO_2 VCD_{trop}, and HCHO VCD_{trop} inverted by Table/Geomtry; (**a**–**c**) is the corresponding frequency variations of the VCDtrop inverted by Model (red line)/Geomtry (blue line); (**d**–**f**) is the normalized frequency distribution and the 25% (green), 50% (red), and 75% (blue) quantile line of relative differences for the VCDtrop.

Figure 7 shows that the consistency of variation trend between the NO_2 (SO_2) VCD_{trop} inverted by Model and that inverted by Geomtry is good, and the relative difference reduces first and then increases with the enhancement of the VCD_{trop}. The overall NO_2 (SO_2, HCHO) VCD_{trop} inverted by Model is slightly greater (less) than that inverted by Geomtry. The relative difference between the inversion of the HCHO VCD_{trop} for Model

and that for Geomtry is greater than that for the VCD_{trop} of NO_2 and SO_2. The sensitivity of the NO_2 VCD_{trop}, HCHO VCD_{trop}, and SO_2 VCD_{trop} for the Model inversion to Geomtry inversion value changes diminishes in turn.

According to Figure 8, corresponding to the frequency variation of the VCDtrop of NO_2, SO_2, and HCHO in the Table/Geometry inversion, the VCDtrop of NO_2 (or SO_2) is mainly concentrated in the range of 1.0 to 4.0 (or 0.5 to 2.5) $\times 10^{16}$ molec/cm^2, while that of HCHO is distributed within the range of 1.5 to 7.5 $\times 10^{16}$ molec/cm^2. The correlation coefficients between the NO_2 (SO_2, HCHO) VCD_{trop} inverted by Table and that inverted by Geomtry is 0.929 (0.836, 0.736) which passed the 99% significance test. The slope and intercept of linear fitting are, respectively, 0.885 (0.700, 0.460) and 0.206 (−0.020, 0.678), and the median relative difference for the VCD_{trop} is −4.44% (−31.28%, −42.52%). When the NO_2 VCD_{trop} inverted by Geomtry is less (greater) than 1.791 $\times 10^{16}$ molec/cm^2, the inversion values of the corresponding Table are slightly larger (smaller). The relative difference between Table and Geomtry decreases (increases) with the increase of the VCD_{trop}, and the overall VCD_{trop} inverted by Table is slightly smaller. When the SO_2 VCD_{trop} inverted by Geomtry is greater than 0.029 $\times 10^{16}$ molec/cm^2, the inversion values of Table increase, and the relative difference between Table and Geomtry gradually diminishes, but the inversion values of Geomtry are always too large. When the HCHO VCD_{trop} inverted by Geomtry is less (greater) than 1.256 $\times 10^{16}$ molec/cm^2, the inversion values of the corresponding Table are slightly larger (smaller). The relative difference between Table and Geomtry decreases (increases) with the increase of the VCD_{trop}. Obviously, the relative difference of the VCD_{trop} between Table/Geomtry inversions are similar to the results of comparative analysis between Model/Geomtry inversions.

Figures 8 and 9 indicate that all of the inversion values of the three algorithms have significant correlation and consistency with changing trends, but there are still certain discrepancies in different gases. The most relative discrepancies exist between the inversion of the HCHO VCD_{trop} for different algorithms, but the relative difference of the SO_2 VCD_{trop} is greater than that of the NO_2 VCD_{trop}. It is likely for this reason that the uncertainty errors introduced are different and are related to the discrepancies in the characteristics, distribution heights, and daily variations of different gases in the atmosphere during the spectral analysis and processing of different gases. The observation near the surface for the MAX-DOAS technology is the most sensitive [13], and the uncertainty of the VCD_{trop} inversion would increase if gases had a higher altitude of concentrated distribution. The calculations of vertical distribution height are based on the concentrations near the surface, so that the greater concentrations would be prone to the errors of the VCD_{trop}. Thus, it can be inferred that the distribution altitude of HCHO is likely one of the reasons why there are greater relative discrepancies for the inversion VCD_{trop} of different algorithms [45]. However, the discrepancy between the relative difference of the NO_2 VCD_{trop} and SO_2 VCD_{trop} is produced by the difference of concentration near the surface and the distribution heights and diurnal variations of NO_2 as well as SO_2. According to comprehensive comparative analysis, the median value of the VCD_{trop} inversion based on Table/Geomtry are greater than that based on Model/Geomtry; that is, the VCD_{trop} inverted by Table is about 10% lower than that inverted by Model. For Model/Table inversion with the same quantile height, the relative differences between the NO_2 VCD_{trop} and SO_2 VCD_{trop} are no more than 4–7% (image omitted).

Figure 9 shows the relationship with seasonal variation in the NO_2 VCD_{trop}, SO_2 VCD_{trop}, and HCHO VCD_{trop} inverted by the three algorithms and the AOD. When the AOD < 1, the greater the inversion the VCD_{trop}, the more difference between the three algorithms, which gradually decreases with the increase in the AOD. When the AOD > 1, the discrepancies of the VCD_{trop} inverted by the three algorithms decline and are relatively stable with the variation in the AOD. It should be considered for this result that the sensitivity of aerosol inverted by MAX-DOAS declines when the AOD increases, so that it leads to the "flattening" effect of a system error on the VCD_{trop} inversion results. The NO_2 (SO_2) VCD_{trop} in autumn is greater than that in winter, and it is the lowest in

summer. The values inverted by Model (Table) are the greatest (lowest), but the inversion values between Table/Geomtry (Model/Geomtry) are relatively consistent. The HCHO VCD_{trop} in summer and autumn is greater than that in winter, and the inversion values of Geomtry, Model, and Table decrease in turn.

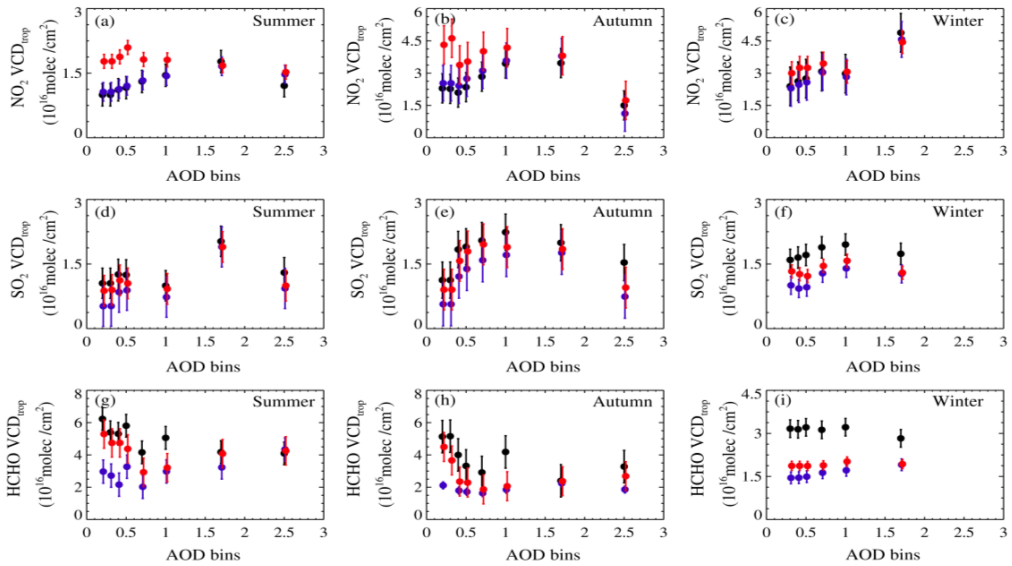

Figure 9. Seasonal variations of three algorithms to invert the relationship of VCD_{trop} with AOD quartiles. (**a**–**c**) denote the relationship of NO_2 VCD_{trop} with AOD quartiles in summer, autumn, and winter, respectively; (**d**–**f**) denote the relationship of SO_2 VCD_{trop} with AOD quartiles in summer, autumn, and winter, respectively; (**g**–**i**) denote the relationship of HCHO VCD_{trop} with AOD quartiles in summer, autumn, and winter, respectively. Geomtry is black, Table is blue, Model is red, and the median of VCD_{trop} is represented by the dots.

It can be noted that the seasonal variations of the HCHO VCD_{trop}, NO_2 VCD_{trop}, and SO_2 VCD_{trop} are different when the aerosol content is low. The HCHO VCD_{trop} inverted by Table is only 1/3 of the Geomtry inversion value, and is only 1/2 of the Model inversion value in summer and autumn. The NO_2 VCD_{trop} inverted by Table is 1/2 of the Model inversion value. The NO_2 VCD_{trop} and SO_2 VCD_{trop} enhance with the increase of aerosol content, but for the HCHO VCD_{trop}, it is the opposite. The changing relationship between the low aerosol content and high HCHO VCD_{trop} shows that a considerable portion of HCHO emissions is likely caused by natural factors. Due to the AOD usually being about 1 at the Qingpu observation station [46,47], there is the greatest difference in the different gas VCD_{trop} values inverted by the three algorithms. Therefore, the relative difference of the VCD_{trop} corresponding to the AOD shows that the VCD_{trop} average inverted by Table is about 25% lower than that by Model, but the relative difference of the NO_2 VCD_{trop}, SO_2 VCD_{trop}, and HCHO VCD_{trop} inversion between Model and Table with the same AOD can reach 8%, 10%, and 7%, respectively. Evidently, the influence of aerosol content on the inversion of the VCD_{trop} is greater than the influence of the vertical distribution height of gas components.

4.3.2. The Variation of Distribution Height

Figure 10 shows the diurnal variations of the vertical distribution height for NO_2 and SO_2 which are inverted by Geomtry in different seasons. The diurnal variation of NO_2 is obvious below a height of 0.5 km, and SO_2 is prone to fluctuate at a height of 0.5 km to 1.0 km, so that the distribution height of NO_2 is lower than that of SO_2. The balloon-borne sounding experiment for Fengxian District, Shanghai, also shows that NO_2 concentrates under 0.6 km [48]. The reason why the distribution height of NO_2 in summer is lower than that in autumn and winter is that NO_2 is prone to photolysis with the increasing

solar radiation in summer; therefore, the distribution height of the NO_2 profile is relatively "shallow" and NO_2 shows a low concentration. By contrast, the distribution height of SO_2 shows an enhancement in summer and a diminishment in winter, which is same as the seasonal variations of aerosol distribution height and boundary layer height. The higher boundary layer height in summer than that in winter is beneficial to the diffusion of SO_2 which has a longer lifespan, so that its distribution height is raised. By comparative analysis, the diurnal variations of the NO_2 and SO_2 vertical distribution heights for different seasons that were inverted by Model and Table, respectively, (image omitted) parallel Figure 11.

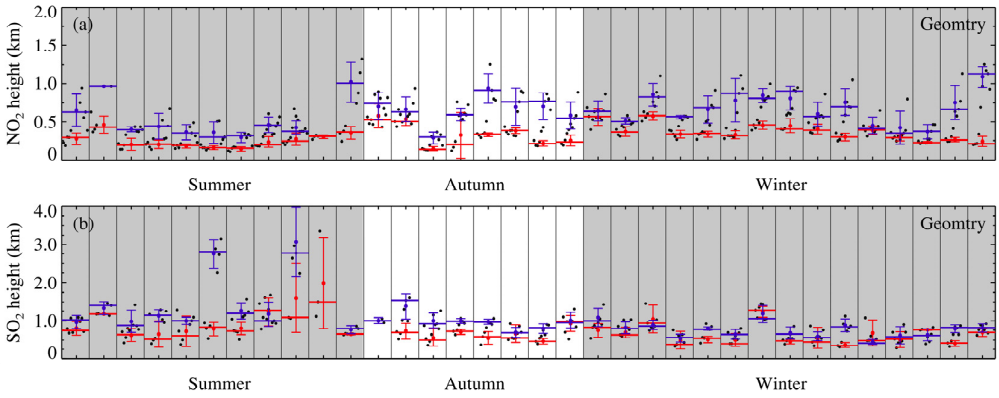

Figure 10. (**a**) Geometric inversion of daily changes in the vertical distribution height of NO_2 in different seasons; (**b**) Geometric inversion of daily changes in the vertical distribution height of SO_2 in different seasons. The hourly average heights are black dots, the distribution height before 10:00 (BJT) is in red, the distribution height after 12:00 (BJT) is in blue, the heights of the median correspond to the blue and red short horizontal lines, respectively, and the points on the error bar are the average heights.

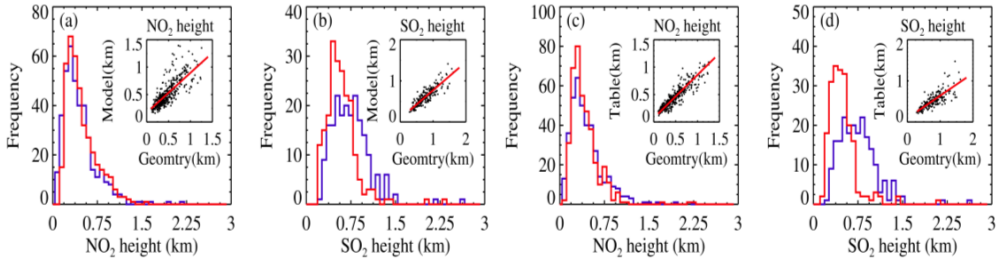

Figure 11. The statistical characteristics of the distribution height for NO_2 and SO_2 inverted by Model/Geomtry (Table/Geomtry); (**a**,**b**), together with (**c**,**d**), are the frequency changes presented by Model (red line)/Geomtry (blue line) and Table (red line)/Geomtry (blue line) for the inversion of NO_2 and SO_2 distribution heights, respectively.

Thus, the diurnal variations of NO_2 and SO_2 show that the distribution heights in the morning are slightly lower than those in the afternoon with different seasons; in the afternoon, the thickening of the boundary layer and the enhancement of turbulent mixing increase their distribution height, and this is similar to the diurnal variation of aerosol distribution height. It can be seen from this that the distribution height of gas components is related to the state where the concentrations near the ground match each other, which is why the consistency of the same gas VCD_{trop} inverted by the three algorithms is better in the afternoon than in the morning. For example, the high concentration and low distribution height of NO_2 near the ground in the morning, especially in the early morning, lead to an increase in the relative differences of the VCD_{trop} inverted by the three algorithms.

In order to compare the relative differences of different gases' distribution heights between the three algorithms' inversion values, Figure 11 shows the frequency variations of distribution height inverted by Model, Table, and Geomtry. Analysis shows that corresponding to the variations in distribution height frequency presented by Model/Geomtry and Table/Geomtry inversion, NO_2 (SO_2) concentrates below the height of 0.5 km (0.8 km) and the relative difference of distribution height between Model and Table inversion increases with the increase in height. The relative difference of the NO_2 distribution height is smaller than that of SO_2. The range of variation in the distribution height for SO_2 inverted by Table is lower than that by Model. When using Table to reflect the concentration changes of SO_2 profiles within a height range of 0.5 to 1 km, it may not represent the real situation but rather "decline" the altitude of the profile [49]. The reason why the relative difference of SO_2 VCD_{trop} inversion between Model and Table is only 8% is that the VCD_{trop} is the integration of the concentration with the distribution height and is not sensitive to the shape of the profile.

The correlation coefficient of the variation in the NO_2 distribution height inverted by Model/Geomtry (Table/Geomtry) is 0.815 (0.919), which passed the 99% significance test; the slope and intercept of the fitting line is 0.729 (0.789) and 0.167 (0.072), respectively; and the median value of the relative difference in distribution height is 10.888% (−3.569%). The overall range of variation in the NO_2 distribution height inverted by Model (Table) is higher (lower) than that by Geomtry, and the distribution height inverted by Model is evidently higher than that by Table. Meanwhile, the inversion height of Geomtry is lower than that of Model (Table) under 0.616 (0.341) km, but higher above 0.616 (0.341) km. The relative difference in the NO_2 distribution height inverted by Model/Geomtry (Table/Geomtry) diminishes first and then enhances with the increase in altitude.

The correlation coefficient of the variation in the SO_2 distribution height inverted by Model/Geomtry (Table/Geomtry) is 0.948 (0.902), which passed the 99% significance test; the slope and intercept of the fitting line is 0.706 (0.694) and 0.068 (−0.021), respectively; and the median value of the relative difference in distribution height is −20.832% (−32.065%). The overall range of variation in the SO_2 distribution height inverted by Model (Table) is lower than that by Geomtry, and the distribution height inverted by Model is evidently higher than that by Table. Meanwhile, the inversion height of Geomtry is higher than that of Model above 0.231 km, but lower under it. The relative difference of the SO_2 distribution height inverted by Model/Geomtry diminishes first and then enhances with the increase in altitude. When the height inverted by Geomtry is above 0.0303 km, the height inverted by Table continuously rises but always remains below Geomtry's height, and the relative difference in inversion height between Table and Geomtry gradually decreases with an increase in height.

Figure 12 shows the seasonal variation in the relationship between the distribution height of NO_2 and SO_2 inverted by the three algorithms with the AOD quantile. Figure 12 indicates that the distribution heights of NO_2 and SO_2 diminish with the increase in the AOD in different seasons. When the AOD < 1, the distribution height of the NO_2 inverted by Model (Geomtry and Table) corresponding to the AOD is relatively high (low), the distribution height of the SO_2 inverted by Table (Geomtry) corresponding to the AOD is low (high), and the distribution height of Model corresponding to the AOD is in the middle. When the AOD > 1, the distribution heights of NO_2 and SO_2 inverted by the three algorithms corresponding to the AOD decline obviously, and the height reduction of NO_2 distribution inverted by Model in autumn is the most significant. The relative differences in the NO_2 and SO_2 distribution heights diminish as the AOD increases because of the fact that an increase in aerosol content can suppress atmospheric convective motion. Obviously, the increase in the AOD also has a "flattening" effect on the distribution heights of different gas components.

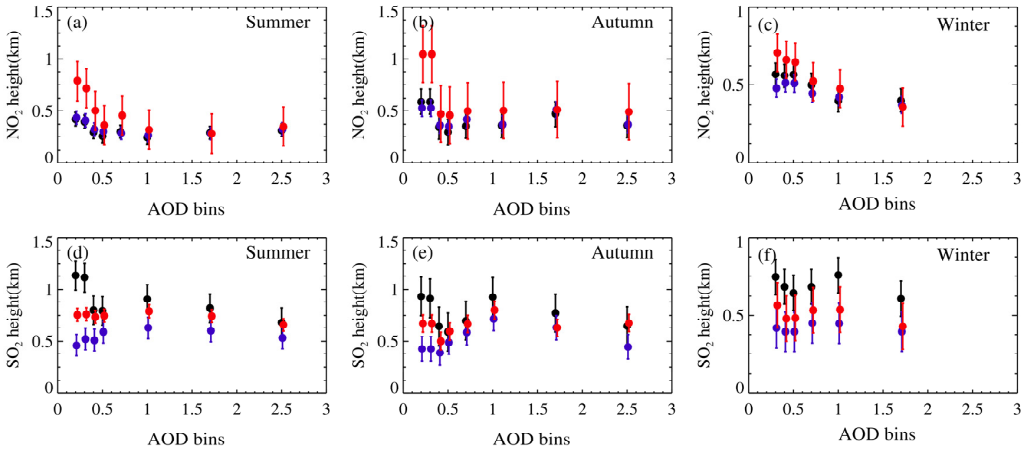

Figure 12. The seasonal variation relationship between the distribution heights of (**a**–**c**) NO_2 and (**d**–**f**) SO_2 with the AOD quantile. Geomtry is black, Table is blue, Model is red, and the dots represent the mid-value of the heights.

4.4. Analysis of Inversion Characteristics of Algorithms

The statistical analyses of the correlation, relative difference, and quantile change of the inversion results for the different algorithms indicate that although there are certain differences between them, all of them can effectively reveal the variation characteristics of seasons, diurnal variations, and distribution heights for different gases' VCD_{trop}. On the one hand, there exists in every algorithm the influence factor of uncertainty which may have a certain impact or cumulative effects on the inversion results in every step of the calculations. For instance, the accuracy of the VCD_{trop} inversion is susceptible to the properties and photochemical characteristics of gas components, the concentration near the surface, distribution height, atmospheric and meteorological conditions, and different configurations of variations between aerosol contents and distribution heights and so forth. The inability to obtain quantitative analytical expressions of these factors leads to uncertainty in the inversion results. On the other hand, it is particularly important that the relative differences between inversion results can be generated by the different settings of aerosol for different algorithms. For example, the setting of aerosols is not considered in Geomtry, and the VCD_{trop} can be quickly and conveniently inverted using only two elevation angles of 30°and 90°. Model needs to divide the aerosol settings into seasons based on different heights, humidity, visibility, and so forth, and uses the same aerosol parameters in the same season, and Table can invert aerosol profiles in real time, which has extremely improved the refinement of aerosol settings compared to Model.

The more concentrated the gases' concentrations within the boundary layer distributed near the surface, the higher the accuracy of the VCD_{trop} inverted by Geomtry. But Geomtry does not consider the influence of aerosol, so it may not be suitable in areas with severe pollution. Statistical analysis indicates that there is an optimum consistency for the NO_2 VCD_{trop} between the three algorithms, and that the relative difference of the NO_2 (SO_2) VCD_{trop} inversion between Model and Table for the quantile of the same heights do not exceed 7% to 15%. Also note that the more intense diurnal variations of gas distribution near the surface and the lower the distribution height, the greater the relative differences of the VCD_{trop} inversion between different algorithms. When the AOD < 0.5, the discrepancy in the NO_2 (HCHO) VCD_{trop} inverted by the three algorithms with AOD quantiles remains significant. When the AOD > 2, the MAX-DOAS causes systematic reduction to the VCD_{trop}. All of this indicates that besides the two internal factors which are the near-surface distributions and vertical distribution heights of gas components, the aerosols are one of the important external factors affecting the inversion of the VCD_{trop}. Therefore, the more precise the setting of aerosols, in principle, the higher the accuracy of the VCD_{trop} inversion. That means this is helpful in enhancing the accuracy of the Table VCD_{trop} inversion.

According to the comparison of the relative differences in the VCD_{trop} in Figures 7 and 8, the peak value of the frequency distribution of the relative difference between Table and Geomtry shows a "left shift" in the negative direction of the horizontal axis relative to Mode/Geomtry. Overall, the VCD_{trop} inverted by Table is slightly smaller, and the relative difference of the VCD_{trop} inversion between Table and Model is 10% on average. The VCD_{trop} inverted by Table is about 25% lower than that by Model for the same AOD quantile. Through mode simulation, the ratio of the VCD_{trop} inverted by Geomtry to the real (simulated) VCD_{trop} is greater than 1, which enhances relative to the increase in the AOD. That means the VCD_{trop} inverted by Geomtry is prone to be overestimated with greater aerosol concentration. Therefore, the settings of the aerosol in Model and Table are indeed a correction to the VCD_{trop} inversion, and the more refined the aerosol settings, the better it is at reducing the overestimation of the VCD_{trop} inversion by MAX-DOAS. Furthermore, there are obvious diurnal variations in the concentration of gas components (including aerosols) in the boundary layer, and Table can describe the diurnal variation characteristics of the VCD_{trop} so that good inversion results can be achieved.

4.5. The Verification and Comparison of MAX-DOAS and the OMI Satellite

We compared the average VCD_{trop} retrieved by MAX-DOAS at the Qingpu observation station within half an hour before and after the OMI satellite transit with the OMI product, and the comparison area was limited within a 50 km range centered around the location of the MAX-DOAS instrument. Figure 13 shows the comparison between the VCD_{trop} inverted by Table for MAX-DOAS and the products corresponding to OMI. According to analysis, the relative coefficients of the NO_2 VCD_{trop}, SO_2 VCD_{trop}, and HCHO VCD_{trop} inversions between the OMI and Table are 0.919, 0.552, and 0.776, and all passed the 99% significance test. The inversion result of Table is slightly higher than the satellite data, and the averages of the NO_2 VCD_{trop}, SO_2 VCD_{trop}, and HCHO VCD_{trop} are 1.1, 2.6, and 1.8 times higher than satellite data, respectively. The reason for the low average VCD_{trop} is the discrepancy in observation methods and spatial and temporal resolutions between the OMI and MAX-DOAS, and the wider scope of OMI observation may contain areas with different levels of pollution. Meanwhile, the observation times between the space-based and ground-based methods are not fully synchronized, MAX-DOAS takes an hourly average, and the OMI is the observed value during transit. In addition, the discrepancy in the AMF caused by different observation methods and that between satellite measurement and MAX-DOAS observation can be simulated by the SCIATRAN model.

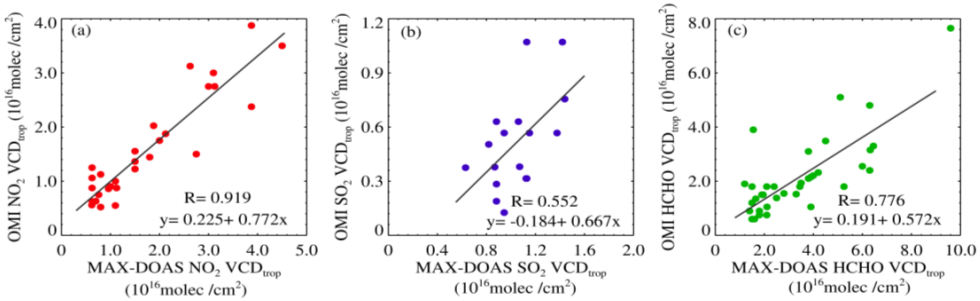

Figure 13. (**a**–**c**) represent the comparison of the MAX-DOAS inverted NO_2 VCD_{trop}, SO_2 VCD_{trop}, and HCHO VCD_{trop} with the corresponding products from the OMI satellite, respectively.

The influence of aerosols during satellite observation is exceedingly important. Taking NO_2 as an example, the sensitivity of satellite observation will decline (enhance) if the aerosol layer is above (below) the NO_2 layer [50]. Our research found that aerosols are mostly concentrated and distributed at an altitude of 1 km, and NO_2 is located near 0.5 km. In order to explore the discrepancy of the AMF between the MAX-DOAS measurement and satellite measurement, in the experimental scheme of the SCIATRAN model, the distribution height of the aerosols is set to 0–1 km, while NO_2 is set to 0–0.3 km and

0–0.5 km, and the AOD values are set to 0, 0.4, 0.8, 1.2, and 1.6. When setting the geometric parameters of MAX-DOAS observation in the model, 30°and 90°elevation angles are used. The elevation and altitude parameters measured by the satellite are set to −90°and the height of the OMI detector is 705 km. The relative azimuth and solar zenith angle are extracted from a combination of satellite transit at 13:30 local time (BJT) in Shanghai.

Substituting all parameters into the SCIATRAN model can simulate the AMF (VCD_{trop}) of MAX-DOAS and the satellite under different settings, which serve as the actual (simulated) AMF (VCD_{trop}) values of MAX-DOAS and the satellite, respectively. In order to facilitate comparison and analysis, only the dAMF value calculated by Geomtry using $dAMF_{30°,trop}/((1 - \sin(30°)/\sin(30°))$ is selected here. The dAMF represents the difference in atmospheric mass factor minus the zenith mass factor of 90° for the MAX-DOAS elevation of 30° (dAMF = dAMF30° − dAMF90°). For satellites, we refer to the AMF calculated by the SCIMACHY detector for standard gas profile inversion (without considering aerosols) as an approximation (APP) [17,51,52]. The ratio of the real AMF to the dAMF of Geomtry (the approximate AMF of the satellite) is the ratio of the VCD_{trop} of Geomtry (satellite) to the real VCD_{trop} (the AMF is inversely proportional to the VCD_{trop}). The ratio being greater than (less than) 1 indicates that the real AMF is larger (smaller) than the approximate AMF or dAMF, while the VCD_{trop} measured by MAX-DOAS or satellite is greater (less) than the real VCD_{trop}. If the ratio is equal to 1, both of them are the real AMF and VCDtrop.

Figure 14 is the ratio between the real AMF and the approximate AMF (dAMF), which is the OMI satellite (MAX-DOAS) corresponding to the NO_2 layer and aerosol layer under different matching scenarios. The result indicates that all of the ratios between the real AMF and the approximate AMF (dAMF), which are the satellite (MAX-DOAS) corresponding to NO_2, are less (greater) than 1. This means that when the NO_2 layer is below the aerosol layer, the VCD_{trop} inverted by MAX-DOAS will be overestimated (higher than the real value), and the products of the OMI will be widely underestimated (lower than the real value). Compared with the SCIMACHY detection, although the NO_2 profile of the OMI products has already been updated and the correction of clouds may append to the algorithms (Jin Junli, 2016), Figure 14 cannot completely represent the relative difference of the NO_2VCD_{trop} measurement between the MAX-DOAS and OMI satellite and it is still possible to semi-quantitatively explain the direct reasons for the discrepancies between the two sets of data. This means that the fundamental reason for the difference between the two observation methods lies in the close relationship between the relative height configuration of the aerosol layer and the NO_2 layer. The results inverted by the three algorithms in MAX-DOAS are about 5~35% higher than the real VCD_{trop}, and those by the OMI are about 20~30% lower than the real VCD_{trop}. At the same time, the greater the AOD, the larger the difference between the dAMF and real AMF; the increasing AOD makes it easier for MAX-DOAS (the OMI satellite) to estimate a high (low) VCD_{trop}. When the AOD is set to less than 1.6, the inversion results can approximately vary about 30% for MAX-DOAS.

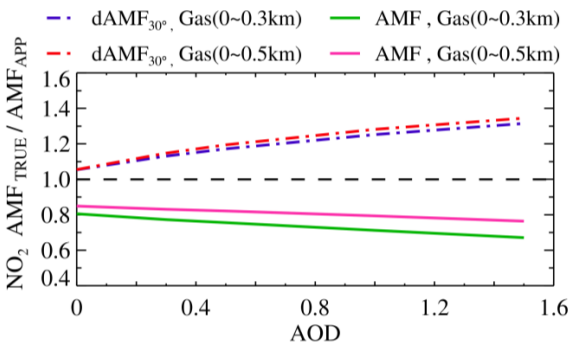

Figure 14. The ratio between the real AMF and the approximate AMF (dAMF) which are the OMI satellite (MAX-DOAS) corresponding to the NO_2 layer and aerosol layer under different matching scenarios.

5. Conclusions

We selected the observed spectra of MAX-DOAS from Qingpu Observatory, Shanghai, and adopted Geomtry, Model, and Table to invert the vertical column concentration of NO_2, SO_2, and HCHO, respectively. We explored the reasons behind and characteristics of the relative differences in the column concentration of inversion between the different algorithms, and obtained the following conclusions:

Among the three inversion algorithms, the calculation results of Geomtry are slightly higher, those of Table are lower, and the calculation results of Model and Table are relatively close. The relative difference in column concentration for the different algorithms was influenced by the diurnal variation that occurred at different vertical distribution heights due to the influence of atmospheric heterogeneity and other factors in the same atmospheric composition. The vertical column concentrations of NO_2 and SO_2 in the afternoon are higher than those in the morning, and different algorithms exhibit good consistency in inverting column concentrations in the afternoon.

The relative difference in the column concentration inverted by the three algorithms are NO_2, SO_2, and HCHO, in descending order. The lower the distribution height of polluting gases, the better the consistency of column concentration inverted by the different algorithms. Comparing the calculation results of Table with the OMI products, there is a significant correlation between them, and the inversion values of MAX-DOAS are higher than those of the OMI products.

Aerosols are an important factor affecting the column concentrations of inversion, and the impact of the AOD on column concentration is greater than that caused by the vertical distribution variation of pollutants in the atmosphere. The maximum deviation between the Geomtry inversion result and the true value did not exceed 35%, and the larger the AOD, the higher the calculation result of Geomtry. Thus, the aerosol settings are corrections to the results inverted by Geomtry. Table can invert aerosol profiles in real time and greatly improve the setting of aerosol refinement compared to Model. The finer aerosol settings are more conducive to reducing the inversion error of MAX-DOAS due to the atmospheric components having obvious diurnal variation characteristics. Therefore, Table can be regarded as an effective algorithm for inverting the VCD_{trop} of NO_2, SO_2, and HCHO.

Author Contributions: Conceptualization, K.Y. and W.W.; methodology, Y.L.; software, K.Y.; validation, K.Y., H.W., and Y.L.; formal analysis, F.X.; investigation, R.G.; resources, K.Y.; data curation, N.Y. and H.W.; writing—original draft, N.Y.; preparation, K.Y.; writing—review and editing, Y.L.; visualization, H.W.; supervision, K.Y.; project administration, H.W.; funding acquisition. All authors have read and agreed to the published version of the manuscript.

Funding: This research was funded by the National Natural Science Foundation of China (grant number 42365007), and funded by the Second Tibetan Plateau Scientific Expedition and Research Program (STEP) (grant number 2019QZKK0604).

Data Availability Statement: The data are not publicly available because the data will be used in future studies.

Acknowledgments: Special thanks to Fudan University for providing MAX-DOAS observations for this study, the SCATRAN radiation transfer model developed by the Remote Sensing Institute of the University of Bremen in Germany, and the QDOAS spectral processing software developed by the Belgian Institute of Space Upper Atmospheric Physics. At the same time, we also would like to thank NASA for providing OMI satellite product data and ECMWF for providing ERA-Interim reanalysis data.

Conflicts of Interest: The authors declare no conflicts of interest.

References

1. Wang, H.Y.; Wei, W.L.; Che, H.Z.; Tang, X.; Bian, J.C.; Yu, K.; Wang, W.G. Ground-based MAX-DOAS measurements of tropospheric aerosols, NO2 and HCHO distributions in the urban environment of Shanghai, China. *Remote Sens.* **2022**, *14*, 1726. [CrossRef]

2. Javed, Z.; Liu, C.; Khokhar, M.F.; Xing, C.; Tan, W.; Subhani, M.A.; Rehman, A.; Tanvir, A. Investigating the impact of Glyoxal retrieval from MAX-DOAS observations during haze and non-haze conditions in Beijing. *J. Environ. Sci.* **2019**, *80*, 296–305. [CrossRef] [PubMed]
3. Benaventa, N.; Garcia-Nieto, D.; Wang, S.S.; Saiz-Lopez, A. MAX-DOAS measurements and vertical profiles of glyoxal and formaldehyde in Madrid, Spain. *Atmos. Environ.* **2019**, *199*, 357–367. [CrossRef]
4. Drosoglou, T.; Koukouli, M.E.; Kouremeti, N.; Bais, A.F.; Zyrichidou, I.; Balis, D.; van der A, R.J.; Xu, J.; Li, A. MAX-DOAS NO_2 observations over Guangzhou, China; ground-based and satellite comparisons. *Atmos. Meas. Tech.* **2018**, *11*, 2239–2255. [CrossRef]
5. Wagner, T.; Beirle, S.; Brauers, T.; Deutschmann, T.; Frieß, U.; Hak, C.; Halla, J.D.; Heue, K.P.; Junkermann, W.; Li, X.; et al. Inversion of tropospheric profiles of aerosol extinction and HCHO and NO_2 mixing ratios from MAX-DOAS observations in Milano during the summer of 2003 and comparison with independent data sets. *Atmos. Meas. Tech.* **2011**, *254*, 2685–2715. [CrossRef]
6. Zhang, C.; Liu, C.; Chan, K.L.; Hu, Q.; Liu, H.; Li, B.; Xing, C.; Tan, W.; Zhou, H.; Si, F.; et al. First observation of tropospheric nitrogen dioxide from the Environmental Trace Gases Monitoring Instrument onboard the GaoFen-5 satellite. *Light Sci. Appl.* **2020**, *9*, 677–685.
7. Khan, W.A.; Khokhar, M.F.; Shoaib, A.; Nawaz, R. Monitoring and analysis of formaldehyde columns over Rawalpindi-Islamabad, Pakistan using MAX-DOAS and satellite observation. *Atmos. Pollut. Res.* **2018**, *9*, 840–848. [CrossRef]
8. Tong, Z.P.; Li, Y.H.; Liu, Y.; Hou, X.G. Spatiotemporal distribution of NO2 in oasis cities between south and north Tianshan Mountains during heavy air pollution. *Environ. Pollut. Control.* **2018**, *41*, 125–132.
9. Lee, H.; Ryu, J.; Irie, H.; Jang, S.-H.; Park, J.; Choi, W.; Hong, H. Investigations of the Diurnal Variation of Vertical HCHO Profiles Based on MAX-DOAS Measurements in Beijing: Comparisons with OMI Vertical Column Data. *Atmosphere* **2015**, *6*, 1816–1832. [CrossRef]
10. Wagner, T.; Dix, B.; Friedeburg, C.V.; Frieß, U.; Sanghavi, S.; Sinreich, R.; Platt, U. MAX-DOAS O4 measurements: A new technique to derive information on atmospheric aerosols—Principles and information content. *J. Geophys. Res. Atmos.* **2004**, *109*, D22205. [CrossRef]
11. Frieß, U.; Monks, P.S.; Remedios, J.J.; Rozanov, A.; Sinreich, R.; Wagner, T.; Platt, U. MAX-DOAS O_4 measurements: A new technique to derive information on atmospheric aerosols: 2. Modeling studies. *J. Geophys. Res. Atmos.* **2006**, *111*, 3007–3021. [CrossRef]
12. Irie, H.; Boersma, F.; Kanaya, Y.; Takashima, H.; Xiaole, P.; Wang, Z. Quantitative bias estimates for tropospheric NO_2 columns retrieved from SCIAMACHY, OMI, and GOME-2 using a common standard for East Asia. *AGU Fall Meet.* **2012**, *5*, 2403–2411.
13. Vlemmix, T.; Hendrick, F.; Pinardi, G.; Smedt, I.D.; Fayt, C.; Hermans, C.; Piters, A.; Wang, P.; Levelt, P.; Roozendael, M.V. MAX-DOAS observations of aerosols, formaldehyde and nitrogen dioxide in the Beijing area: Comparison of two profile retrieval approaches. *Atmos. Meas. Tech.* **2015**, *8*, 941–963. [CrossRef]
14. Friedeburg, C.V.; Pundt, I.; Mettendorf, K.U.; Wagner, T.; Platt, U. Multi-axis-DOAS measurements of NO_2 during the BAB II motorway emission campaign. *Atmos. Environ.* **2005**, *39*, 977–985. [CrossRef]
15. Brinksma, E.J.; Pinardi, G.; Volten, H.; Braak, R.; Richter, A.; Schönhardt, A.; Van Roozendael, M.; Fayt, C.; Hermans, C.; Dirksen, R.J.; et al. The 2005 and 2006 DANDELIONS NO_2 and aerosol intercomparison campaigns. *J. Geophys. Res. Atmos.* **2008**, *113*, 762–770. [CrossRef]
16. Honninger, G.; Von Friedeburg, C.; Platt, U. Multi axis differential optical absorption spectroscopy (MAX-DOAS). *Atmos. Chem. Phys.* **2004**, *4*, 231–254. [CrossRef]
17. Ma, J.Z.; Beirle, S.; Jin, J.L.; Shaiganfar, R.; Yan, P.; Wagner, T. Tropospheric NO_2 vertical column densities over Beijing: Results of the first three years of ground-based MAX-DOAS measurements (2008–2011) and satellite validation. *Atmos. Chem. Phys.* **2013**, *13*, 1547–1567. [CrossRef]
18. Wang, T.; Wang, P.C.; Yu, H.; Zhang, X.Y.; Zhou, B.; Si, F.Q.; Wang, S.S.; Bai, W.G.; Zhou, H.J.; Zhao, H. Intercomparison of slant column measurements of NO_2 by ground-based MAX-DOAS. *Acta Phys. Sin.* **2013**, *62*, 054206. [CrossRef]
19. Wang, T.; Wang, P.C.; Yu, H.; Sun, L. Analysis of the Characteristics of tropospheric NO_2 in Xianghe based on MAX-DOAS measurement. *Clim. Environ. Res.* **2014**, *19*, 51–60.
20. Fu, Q.; Liu, W.Q.; Ci, F.Q.; Zhang, Y.H.; Xie, P.H. Determination of the vertical column density of trace gas measured by MAX-DOAS. *Acta Photonica Sin.* **2009**, *38*, 1216–1220.
21. Wu, F.C.; Li, A.; Xie, P.H.; Chen, H.; Ling, L.Y.; Xu, J.; Mou, F.S.; Zhang, J.; Shen, J.C.; Liu, J.G.; et al. Dectection and distribution of tropospheric NO_2 vertical column density based on mobile multi-axis differential optical absorption spectroscopy. *Acta Phys. Sin.* **2015**, *64*, 198–208. [CrossRef]
22. Li, X.; Brauers, T.; Hofzumahaus, A.; Lu, K.; Li, P.Y.; Shao, M.; Wanger, T.; Wahner, A. MAX-DOAS measurements of NO_2, HCHO and CHOCHO at a rural site in Southern China. *Atmos. Chem. Phys.* **2013**, *13*, 2133–2151. [CrossRef]
23. Li, X.; Brauers, T.; Shao, M.; Garland, R.M.; Wagner, T.; Deutschmann, T.; Wahner, A. MAX-DOAS measurements in southern China: Retrieval of aerosol extinctions and validation using ground-based in-situ data. *Atmos. Chem. Phys.* **2010**, *10*, 2079–2089. [CrossRef]
24. Platt, U.; Stutz, J. *Differential Optical Absorption Spectroscopy, Physics of Earth and Space Environments*; Springer: Berlin/Heidelberg, Germany, 2008.

25. Hendrick, F.; Müller, J.F.; De Mazière, M.; Fayt, C.; Gielen, C.; Hermans, C.; Ma, J.Z.; Pinardi, G.; Stavrakou, T.; Vlemmix, T.; et al. Four Years of Ground-based MAX-DOAS Observations of HONO and NO_2 in the Beijing Area. *Atmos. Chem. Phys.* **2013**, *14*, 765–781. [CrossRef]
26. Jin, J.; Ma, J.; Lin, W.; Zhao, H.; Shaiganfar, R.; Beirle, S.; Wagner, T. MAX-DOAS measurements and satellite validation of tropospheric NO_2 and SO_2 vertical column densities at a rural site of North China. *Atmos. Environ.* **2016**, *133*, 12–25. [CrossRef]
27. Chen, Z.; Wang, G.; Wang, D.; Si, F.K. Analysis on change characteristic of autumn relative humidity in China. *Mod. Agric. Sci. Technol.* **2017**, *6*, 173–174.
28. Wang, Y.D.; Wang, Z.X. Characteristics of PM2.5 concentration variability and its meteorological factors in Shanghai. *Arid. Land Geogr.* **2018**, *41*, 1088–1096. [CrossRef]
29. Wang, S.S. Inversion Study of NO_2 and Aerosol Pollution in Shanghai Urban Area Based on Passive DOAS. Master's Thesis, Fudan University, Shanghai, China, 2012.
30. Duan, Y.S. Shanghai Atmospheric Visibility Study. Master's Thesis, East China Normal University, Shanghai, China, 2005.
31. Shi, H.; Chen, M.; Han, J.J. Analysis of factors affecting visibility and its variation features in Pudong area of Shanghai. *Atmos. Sci. Res. Appl.* **2008**, *2*, 1–8.
32. Li, Y.J.; Shu, J. Study of horizontal visibility in Shanghai by PWD22. Adm. *Tech. Environ. Monit.* **2010**, *22*, 24–28.
33. Yao, J.; Liu, W.; Wang, G.H.; Zeng, Y.S.; Huang, Y.; Liu, S.Q.; Yuan, N. The variation characteristics of atmospheric visibility in Jiading District, Shanghai. *Environ. Pollut. Control.* **2013**, *35*, 36–41.
34. Fried, A.; Crawford, J.; Olson, J.; Walega, J.; Potter, W.; Wert, B.; Jordan, C.; Anderson, B.; Shetter, R.; Lefer, B.; et al. Airborne tunable diode laser measurements of formaldehyde during TRACE-P: Distributions and box model comparisons. *J. Geophys. Res.* **2003**, *108*, 8798. [CrossRef]
35. Junkermann, W. On the distribution of formaldehyde in the western Po-Valley, Italy, during FORMAT 2002/2003. *Atmos. Chem. Phys.* **2009**, *9*, 9187–9196. [CrossRef]
36. Klippel, T.; Fischer, H.; Bozem, H.; Lawrence, M.G.; Butler, T.; Jöckel, P.; Tost, H.; Martinez, M.; Harder, H.; Regelin, E.; et al. Distribution of hydrogen peroxide and formaldehyde over Central Europe during the HOOVER project. *Atmos. Chem. Phys.* **2011**, *11*, 4391–4410. [CrossRef]
37. Tian, X.; Xie, P.; Xu, J.; Li, A.; Wang, Y.; Qin, M.; Hu, Z. Long-term observations of tropospheric NO_2, SO_2 and HCHO by MAX-DOAS in Yangtze River Delta area, China. *J. Environ. Sci.* **2018**, *71*, 210–224. [CrossRef]
38. Jin, J.L.; Ma, J.Z.; Lin, W.Z.; Zhao, H.R. Characteristics of NO2 tropospheric column density over a Rural area in the North China Plain. *J. Appl. Meteorol. Sci.* **2016**, *27*, 303–311.
39. Fu, T.M.; Jacob, D.J.; Palmer, P.I.; Chance, K.; Wang, Y.X.; Barletta, B.; Blake, D.R.; Stanton, J.C.; Pilling, M.J. Space-based formaldehyde measurements as constraints on volatile organic compound emissions in east and south Asia and implications for ozone. *J. Geophys. Res. Atmos.* **2007**, *112*, D06312. [CrossRef]
40. Barkley, M.P.; Kurosu, T.P.; Chance, K.; Smedt IDe Roozendael, M.V.; Arneth, A.; Hagberg, D.; Guenther, A. Assessing sources of uncertainty in formaldehyde air mass factors over tropical South America: Implications for top-down isoprene emission estimates. *J. Geophys. Res. Atmos.* **2012**, *117*, D13304. [CrossRef]
41. Li, X.; Wang, S.; Zhou, R.; Zhou, B. Urban atmospheric formaldehyde concentrations measured by a differential optical absorption spectroscopy method. *Environ. Sci. Process. Impacts* **2014**, *16*, 291–297. [CrossRef]
42. Chen, D. Study on Atmospheric Trace Gas Measurements Using Zenith-Sky Scattered Light-DOAS Technique. Master's Thesis, Fudan University, Shanghai, China, 2008.
43. Yang, S.N. Study on Atmospheric Pollution in Shanghaiusing Zenith-Sky Passive DOAS Technique. Master's Thesis, Fudan University, Shanghai, China, 2011.
44. Chan, K.L.; Hartl, A.; Lam, Y.F.; Xie, P.H.; Liu, W.Q.; Cheung, H.M.; Lampel, J.; Pohler, D.; Li, A.; Xu, J.; et al. Observations of tropospheric NO_2 using ground based MAX-DOAS and OMI in measurements during the Shanghai World Expo 2010. *Atmos. Environ.* **2015**, *119*, 45–58. [CrossRef]
45. Tian, X.; Xu, J.; Xie, P.H.; Li, A.; Hu, Z.K.; Li, X.M.; Ren, B.; Wu, Z.Y. Retrieving tropospheric vertical distribution in HCHO by multi-Axis differential optical absorption spectroscopy. *Spectrosc. Spectr. Anal.* **2019**, *39*, 2325–2331.
46. Cheng, T.; Xu, C.; Duan, J.; Wang, Y.; Leng, C.; Tao, J.; Che, H.; He, Q.; Wu, Y.; Zhang, R.; et al. Seasonal variation and difference of aerosol optical properties in columnar and surface atmospheres over Shanghai. *Atmos. Environ.* **2015**, *123*, 315–326. [CrossRef]
47. Zhang, J.; Wang, S.; Guo, Y.; Zhang, R.; Qina, X.; Huang, K.; Wang, D.; Fud, Q.; Wang, J.; Zhou, B. Aerosol vertical profile retrieved from ground-based MAX-DOAS observation and characteristic distribution during wintertime in Shanghai, China. *Atmos. Environ.* **2018**, *192*, 193–205. [CrossRef]
48. Xing, C.; Liu, C.; Wang, S.; Chan, K.L.; Gao, Y.; Huang, X.; Su, W.; Zhang, C.; Dong, Y.; Fan, G.; et al. Observations of the vertical distributions of summertime atmospheric pollutants and the corresponding ozone production in Shanghai, China. *Atmos. Chem. Phys.* **2017**, *17*, 14275–14289. [CrossRef]
49. Wang, Y.; Lampel, J.; Xie, P.; Beirle, S.; Li, A.; Wu, D.; Wagner, T. Ground-based MAX-DOAS observations of tropospheric aerosols, NO2, SO2 and HCHO in Wuxi, China, from 2011 to 2014. *Atmos. Chem. Phys.* **2017**, *17*, 2189–2215.
50. Leitao, J.; Richter, A.; Vrekoussis, M.; Kokhanovsky, A.; Zhang, Q.J.; Beekmann, M.; Burrows, J.P. On the improvement of NO_2 satellite retrievals—Aerosol impact on the airmass factors. *Atmos. Meas. Tech.* **2010**, *3*, 475–493. [CrossRef]

51. Liu, C.; Bai, W.G.; Zhang, X.Y.; Zhang, P. An improvement of retrieving carbon monoxide from SCIAMACHY Part I: With respect to the instrumenta1 issues. *Chin. J. Geophys.* **2013**, *56*, 758–769. (In Chinese)
52. Jin, J.L. MAX-DOAS measurements of tropospheric NO_2 and SO_2 vertical column densities over atypical polluted area in North China. Ph.D. Thesis, Chinese Academy of Meteorological Sciences, Beijing, China, 2016.

Disclaimer/Publisher's Note: The statements, opinions and data contained in all publications are solely those of the individual author(s) and contributor(s) and not of MDPI and/or the editor(s). MDPI and/or the editor(s) disclaim responsibility for any injury to people or property resulting from any ideas, methods, instructions or products referred to in the content.